Open Fan Noise Confinement Effects in a Closed Wind-Tunnel: Numerical Methodology and Evaluation

Mathieu Lorteau, Thomas Le Garrec, Vincent Daydé-Thomas

Open Fan noise confinement effects in a closed wind-tunnel: numerical methodology and evaluation

Mathieu Lorteau*, Thomas Le Garrec†
DAAA, ONERA, Institut Polytechnique de Paris
92320 Châtillon - France

Vincent Daydé-Thomas‡
Safran Aircraft Engines, Rond-point René Ravaud, Moissy-Cramayel, France

This work investigates, through numerical simulations, the acoustic confinement effects of an open fan test bench installed in a wind-tunnel with closed test section. The present activity makes use of the full IBM methodology developed in previous work, which consists in computing with a CAA solver, the propagation of the acoustic waves generated by an Open Fan acoustic source model injected in the CAA domain, in the presence of complex geometries and a realistic non-uniform mean flow previously obtained with a CFD solver. The CAA solver uses the Immersed Boundary Method (IBM) to deal with the bench and wind-tunnel geometries, which greatly simplifies the grid generation process and also drastically reduces the overall computational time.

Two simulations are performed for an operating point corresponding to a take-off condition: a free-field and a confined configuration with rigid walls. Despite strong reflected waves from the wind-tunnel walls, the free-field directivity can still be retrieved for the main directions of radiation.

I. Introduction

In the recent years, engine fuel consumption and CO_2 emissions have been the subject of an increasing number of research studies and continuous improvements were achieved by engine manufacturers, notably by increasing the fan's bypass ratio. To go a step beyond the progresses already achieved, the Open Fan or Unducted Single Fan (USF) architecture represents one of the solution of interest. However, due to ever more restrictive noise regulations around airports, acoustic certification of such an engine architecture are all the more necessary. Acoustics is taken into account in the early development of new architecture. Moreover, an important key point to reduce aircraft noise consists in the understanding of the physical mechanisms behind the noise generation process. In this context, it is necessary to have access to reliable experimental and numerical database, in particular on the engine noise related to the rotating parts which constitutes nowadays a growing acoustic source of an aircraft.

The present study focuses on the Open Fan noise confinement effects in an aerodynamic wind-tunnel. To this aim, the methodology first implemented by Mincu *et al.* [1] and further improved by Lorteau *et al.* [2–4] is used. Here, the Immersed Boundary Method (IBM) workflow implemented in the CAA solver *sAbrinA* [5–9] is used to study the acoustic confinement in a closed aerodynamic wind-tunnel of the noise radiated by a Open Fan bench with a realistic bench geometry in presence of a realistic mean flow at a Mach number corresponding to take-off flight conditions. To this aim, we compare the tonal acoustic field from the same fan bench in the confined configuration and in free-field for the first BPFs. Both acoustic fields are obtained from the same methodology. Firstly, a realistic mean flow is computed around the geometry under consideration. Secondly, this mean flow is interpolated on the CAA grid and used afterwards in the CAA computation in which we consider a novel acoustic sources modelling for tonal noise associated to Open Fan architecture [10, 11] to compute the acoustic source near field.

This paper is organized as follows. In section II, the methodology used in this paper to evaluate the acoustic confinement effects is briefly presented, some details are given on both the CFD and CAA computations. Then, section III provides details on the acoustic source used in this work: the acoustic sources modelling as well as how the model is injected into the CAA, with numerical validations on a simpler test case. The acoustic confinement effects

*Research engineer, Aerodynamics, Aeroelasticity and Acoustics Department, mathieu.lorteau@onera.fr
†Research engineer, Aerodynamics, Aeroelasticity and Acoustics Department, thomas.le_garrec@onera.fr
‡PhD student, vincent.dayde-thomas@safrangroup.com

numerical evaluation is presented in section IV. The latter section includes details on the numerical parameters and analysis of wind-tunnel wall effects on sound directivity from the Open Fan mock-up with respect to reference free-field simulation. Finally, some conclusions and perspectives are given in section V.

II. Numerical methodology

In order to estimate the acoustic confinement effects of an Open Fan test bench in a wind-tunnel, we intend to compute the noise radiated by this Open Fan taking into account the wind-tunnel geometry and the mean flow effects by means of CAA. The CAA computations are performed with ONERA's structured solver *sAbrinA* [5–9] for which an IBM methodology has been developed. The full IBM methodology can be found in Mincu *et al.*[1] and has been applied in Lorteau *et al.* [2]. This IBM methodology has been recently successfully applied in Lorteau & Le Garrec [3] for a similar study as the present one but for turbofan noise.

For the CAA computations, the geometry of interest is taken into account with the IBM approach, which thus greatly simplifies the CAA mesh design process for such a geometry, the mesh simply consisting in a single 3D Cartesian grid. The acoustic source modelling used for USF tonal noise in this study is presented in the following section.

The heterogeneous mean flow, issued from a RANS computation, is interpolated from the CFD grid to the CAA grid by the use of the in-house *Cassiopée* tool [12]. The CAA computation is then performed in the temporal domain, and thus including all the frequencies under consideration in a single computation, to propagate the waves radiated by the acoustic source on the mean flow from the vicinity of the test bench up to wind-tunnel walls. Besides a great simplification of the mesh generation process, the IBM approach also allows to maximize the time step (as a body fitted curvilinear mesh is not needed around the bench geometry) and thus minimize the computational time to get a prescribed signal length to compute statistics. More information on the solvers used for the CFD and CAA steps are provided in sections IV.A and IV.B.

III. Acoustic sources

A. Source injection methodology

1. USF source model

In the framework of a PhD thesis funded by Safran Aircraft Engines (SAE) and supervized by ONERA and ENSAM (DynFluid), a source model devoted to the characterization of the tone noise radiation generated by the propeller blades and the stator vanes of a USF has been developed at ONERA in Daydé-Thomas *et al.* [10, 11]. This model is classically based on the Ffowcs Williams and Hawkings (FWH) analogy limited to thickness noise and loading noise terms, written in the frequency domain, and using a source-mode approach as done by Roger & Kucukcoskun [13]. It is thus restricted to blade/vane sources and should be relevant for subsonic conditions (without shocks), since the quadrupole volume sources are not taken into account. This simple principle, also proposed by Polacsek *et al.* [6], traduces the fact that the noise emitted by a rotating source can be equivalently expressed as a continuous distribution of fixed phase-shifted sources placed circularly around the revolution axis. The phase shift is directly linked to the angular (spinning) mode order m, associated to the blade passing frequencies (BPFs).

This source-mode approach has been validated against Ffowcs Williams and Hawkings time-domain computations performed with reference solutions issued from a solid surface time-domain FWH formulation available in the ONERA's *KIM* solver [14]. In figure 1, the directivity obtained with the USF source model has been compared with KIM solutions for a take-off operating point at BPF1 for the rotor and stator loading noise.

2. Sound field injection over NRI surfaces

The USF source model can be injected using the Non-Reflective Interface (NRI) which is a forcing technique enabling the injection of incoming sound field into the CAA domain through a silent interface. Unlike most existing forcing techniques, the NRI is acoustically "transparent" in nature and, therefore, can properly handle the backscattering effects arising during the noise propagation step. More details about the NRI technique can be found in [15]. This technique has been recently applied in [4, 16] to the study of fan noise propagation outside of the nacelle to evaluate propagation effects in presence of a non uniform mean flow and the aircraft geometry.

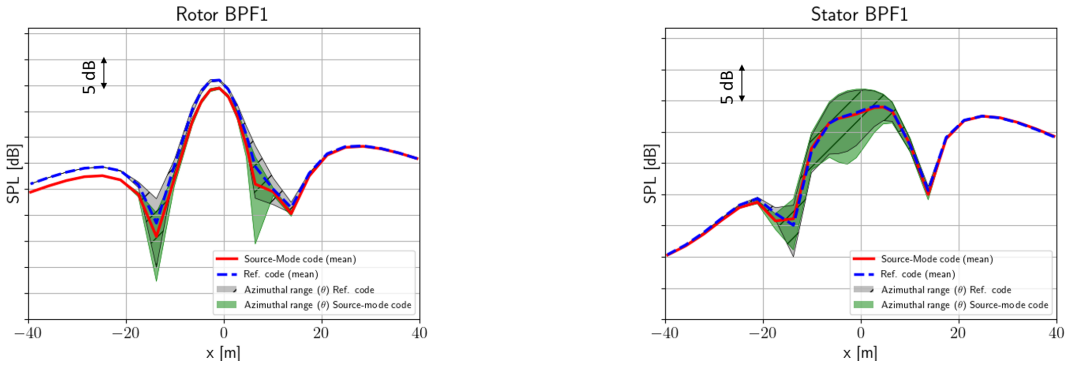

(a) (b)

Fig. 1 Comparison between the source-mode approach and FWH predictions in terms of loading noise directivities obtained at take-off conditions and at BPF1 for (a) the rotor and (b) the stator.

3. Reconstruction of conservative variables (from acoustic pressure inputs)

In order to inject in *sAbrinA* the present acoustic source model via the above mentioned NRI technique involving non-conservative variables, acoustic pressure, acoustic velocity and density fluctuations are required. The pressure data are directly provided by the USF source model, however the velocity data need to be assessed by other means (the density fluctuation being directly related to the pressure fluctuation using the standard isentropic assumption). As presented in section III.A.1 the model relies on linear acoustics and a uniform mean flow hypothesis. Under these assumptions, the acoustic pressure p and velocity $\overrightarrow{u}$ can be related to the acoustic potential ϕ by the following relations, in the frequency domain:

$$\begin{cases} \overrightarrow{u} = \overrightarrow{\nabla}\phi \\ p = -\rho_0 \left(i\omega\phi + \overrightarrow{U}_\infty . \overrightarrow{\nabla}\phi \right) \end{cases} \tag{1}$$

In the equations above, ρ_0 represents the reference density and $\omega = 2\pi f$ the pulsation related to the frequency f. In the case of a uniform mean flow $\overrightarrow{U_\infty} = U_\infty \overrightarrow{e_x}$ in the x direction, the acoustic pressure writes as:

$$p = -\rho_0 \left(i\omega\phi + U_\infty . \frac{\partial \phi}{\partial x} \right) \tag{2}$$

The equation 2 above is a first order partial derivative equation corresponding to an advection equation in the frequency domain for the scalar field ϕ function with a source term p (the data p are known). A solution of equation 2 is:

$$\phi(x) = \frac{-1}{\rho_0 U_\infty} e^{-i\omega/U_\infty x} \int_{x_0}^{x} p(s) e^{i\omega/U_\infty s} ds + \phi(x_0) e^{-i\omega/U_\infty (x - x_0)} \tag{3}$$

Where x_0 corresponds to a position where the acoustic potential is known. If x_0 is sufficiently far away from the acoustic source, then $\phi(x_0)$ tends toward 0 and the analytical expression of the acoustic potential reduces to the evaluation of an 1D integral only with known pressure data. For cases where x_0 is close to the source so that $\phi(x_0)$ can not be considered null, then a filtering procedure has to be applied to eliminate the oscillations related to the term $\phi(x_0) e^{-i\omega/U_\infty (x - x_0)}$ in the above equation. Once the acoustic potential is obtained from equation 3, the acoustic velocity can be derived from the acoustic potential spatial derivatives (see equation 1).

B. First acoustic validations

In this section, the reconstruction method presented in section III.A.3 is first assessed for the case of a monopolar source in a uniform mean flow for which the analytical solution is known. Secondly, the reconstruction method is applied to the USF source model presented in section III.A.1. The reconstructed data are then injected into preliminary CAA computations performed with the solver *sAbrinA* with a uniform mean flow. The CAA results are finally compared directly to results provided by the same USF source model.

1. Reconstruction method validation: source-point academic case

To assess its validity, the reconstruction method, proposed in section III.A.3, is applied to the test case of a monopolar source at the frequency $f = 140$ Hz in a uniform mean flow in the x direction at a Mach number M = 0.2.

A color maps comparison of the real part of the pressure fluctuations, acoustic potential and velocity fields between the reconstruction method and the analytical solution in a longitudinal plane is presented in figure 2, at the same frequency $f = 140$ Hz. It appears that the results derived from the reconstruction method perfectly match with the analytical solution. Nonetheless, some slight discrepancies can be observed close to the source location as for these locations, the amplitude is infinite.

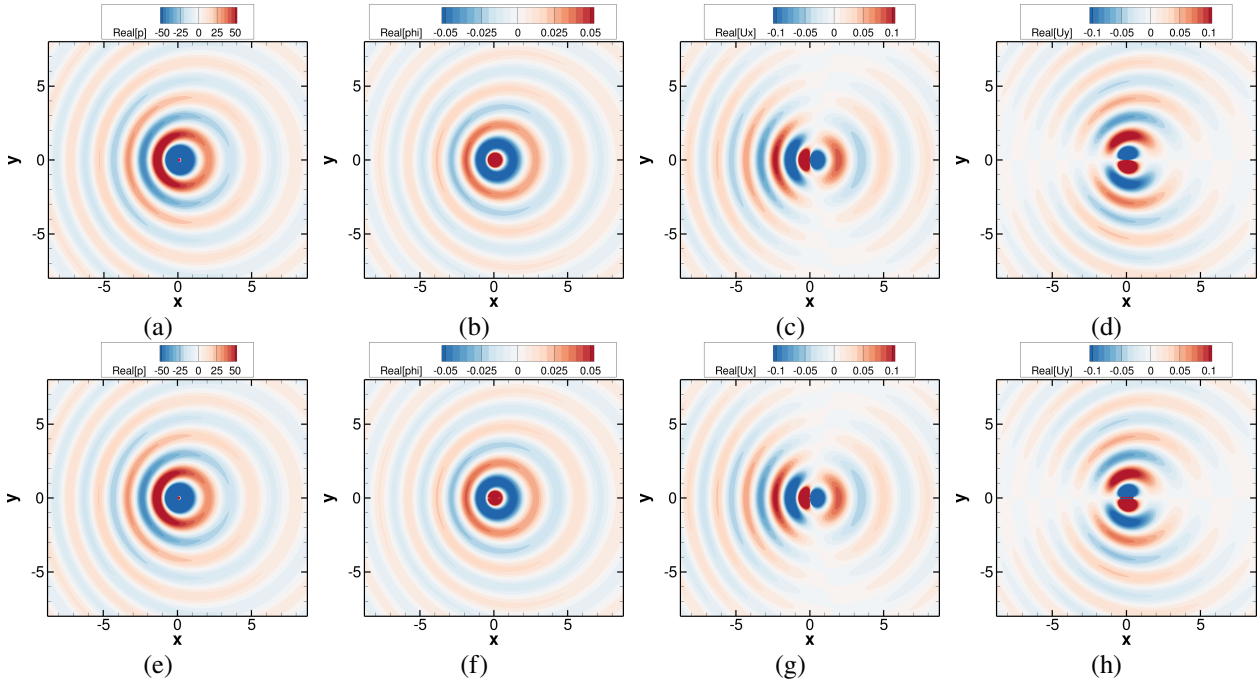

Fig. 2 Real part of the fluctuating pressure (a, e), the acoustic potential (b, f), the x-velocity (c, g) and y-velocity (d, h) fields of a monopolar source at $f = 140$ Hz and with a uniform mean flow at M $= 0.2$ in the z=0 plane. Top: the analytical expression; bottom: the reconstruction method.

In figure 3, more accurate quantitative comparisons are drawn on a longitudinal line y=2m and z=0 for the same variables. Predictions resulting from the reconstructed method match the analytical solution for all the variables. The mesh discretization has been chosen so that the acoustic velocity components derived from the spatial derivatives of the acoustic potential have a sufficiently low discretization error.

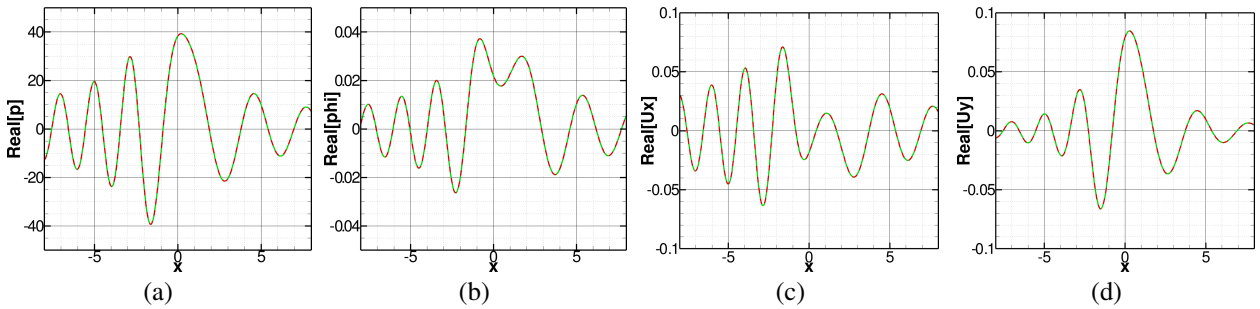

Fig. 3 Comparison at y=2m and z=0 of the longitudinal evolution of the real part of the fluctuating pressure (a), the acoustic potential (b), the x-velocity (c) and the y-velocity (d) levels of a monopolar source at $f = 140$ Hz and M $= 0.2$. analytical expression, – – –; reconstruction method, ——.

These results give a first validation of the reconstruction method. In the next step, CAA predictions are performed with the actual USF source model through the NRI technique.

2. First CAA simulation: isolated USF loading noise

The USF source model has been applied to data provided by a URANS CFD simulation with the chorochronic approach and performed on a USF configuration corresponding to an approach condition at a flight Mach number around 0.22 and a rotor rotation of approximately 600 rpm, see Sugiyama *et al.* [17] for more details on the CFD simulations. The geometry is the one considered in the DGAC project INPRO and is studied in [17–19]. The source model from [10, 11] can provide acoustic pressure levels for both the steady and unsteady loading noises.

For these first CAA simulations, both of these steady and unsteady loading noise terms discussed in section III.A.1 have been tested separately at BPF1. The focus is put on the unsteady loading noise component as it is the main contributor for this operating point.

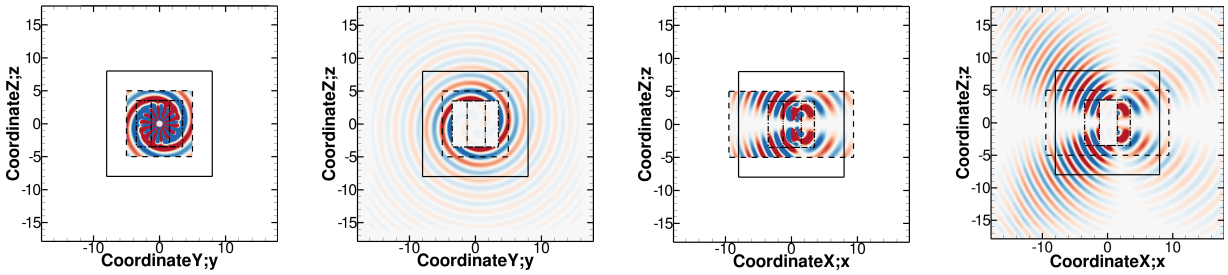

(a) (b) (c) (d)

Fig. 4 Real part of the fluctuating pressure field associated to BPF1 for the unsteady loading noise in the x=0 plane (a, b) and the y=0 plane (c, d) for the source model (a, c) and the CAA simulation (b, d). The solid line (——) corresponds to the CAA refined mesh zone boundaries, the dashed line (− − −) to the source model input boundaries and the dash-dotted (− · − ·) and dash-dot-dotted (− ·· − ··) lines to the NRI surface boundaries.

The comparisons presented in figure 4 between fluctuating pressure values provided directly by the model and obtained by propagation of the data by the CAA solver *sAbrinA* show that the acoustic pressure obtained with *sAbrinA* is propagated accordingly to the USF source model. The excellent agreement between the pressure levels obtained on 8 m radius arcs of microphones by the two approaches, and depicted in figure 5, confirms this finding. Furthermore, the agreement of the real and imaginary parts of the fluctuating pressure levels demonstrates that the phase information is fairly well preserved.

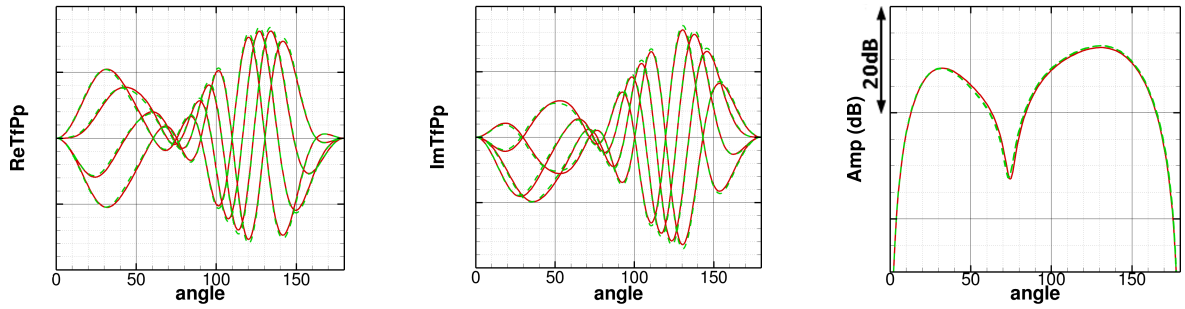

(a) (b) (c)

Fig. 5 Comparison on four 8 m radius arcs of microphones of the real (a), the imaginary parts (b) and the amplitude in dB (c) of the fluctuating pressure field at BPF1 for the unsteady loading noise. USF source model, − − −; CAA simulation, —— .

In figure 6, similar comparisons obtained for steady loading noise are presented. For this noise component, the acoustic waves are also propagated in the same way as the USF source model. Some discrepancies can nonetheless be noticed at angles around 50° and 130°, i.e. on each side of the main radiation peak at 90°. Given the dynamic of more than 40 dB, these discrepancies can be associated to numerical dissipation. This validates the approach for both the unsteady and steady loading noise at BPF1.

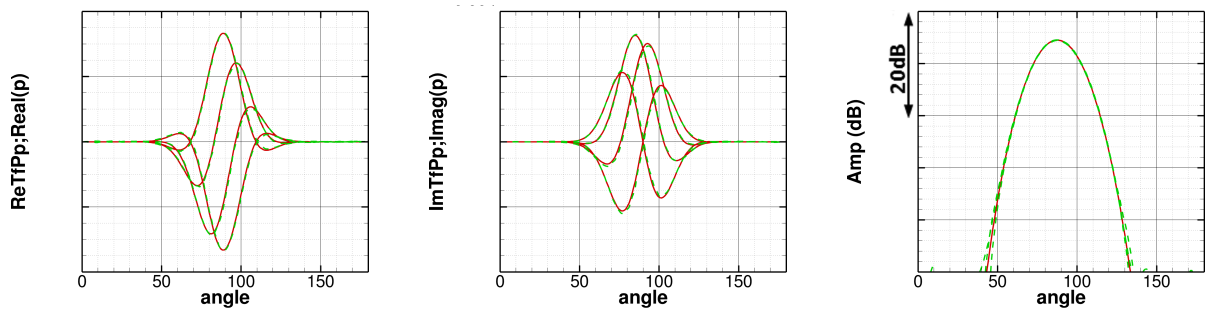

(a) (b) (c)

Fig. 6 Comparison on four 8 m radius arcs of microphones of the real (a), the imaginary parts (b) and the amplitude in dB (c) of the fluctuating pressure field associated to BPF1 for the steady loading noise. USF source model, – – –; CAA simulation, ——.

IV. Acoustic confinement effects evaluation

In this section, the acoustic confinement effects of a USF test bench in an aerodynamic wind-tunnel are evaluated using the numerical method presented in section II and the source modelling in section III.A.1. First, the numerical parameters considered for the simulations (operating condition, mesh, etc.) are given. Then, the acoustic results obtained for the confined simulation are compared to the free-field ones in terms of directivity to evaluate how much and for which angular positions the confinement effects have an impact on the acoustic levels. Except for the source modelling and its injection into the CAA solver, the numerical methodology is very similar to the one employed in Lorteau & Le Garrec [3] for the assessment of fan noise confinement effects in a closed wind-tunnel.

A. Geometry and operating condition

The acoustic confinement effects are evaluated in a generic aerodynamic wind-tunnel with a test section of $22D_b$ in diameter and $33D_b$ in length (with D_b the rotor blade length). As mentioned in section III.A.2, the source model is injected using the NRI technique which relies on a $2D_b \times 3.5D_b \times 3.5D_b$ rectangular surface encompassing the acoustic sources, i.e. the rotor and the stator of the USF test bench. Therefore, the USF geometry does not need to be included in the CAA simulation. However, for the simulations presented in the following, a generic support located around $1.5D_b$ below the wind-tunnel test section axis has been considered.

For this study, a take-off operating point has been considered with a flight Mach number around 0.29 and a rotor rotation of approximately 1000rpm. Similarly to section III.B.2, the USF source model has been applied to data provided by a URANS CFD simulation (see [17] for more details). For these simulations, the unsteady loading noise for both the rotor and stator and the steady loading noise for the rotor are injected at the frequencies BPF1 and BPF2.

The non uniform mean flow considered here has been computed (and provided to ONERA) by SAE using ONERA's solver *elsA*[20] with a RANS approach on an unstructured grid. It should be noted that a simple through-flow condition is used around the test bench, as the rotor/stator stage is not modelled. Only one flow field was computed which corresponds to the confined case. This flow field was also used for the free-field case with the boundary layer at the wind-tunnel walls removed. This will remove any bias related to the mean flow for the results comparisons between the confined case and the free-field case.

B. Acoustic mesh characteristics and numerical parameters

The CAA calculations are conducted with ONERA's *sAbrinA* structured CAA solver that solves either the full or the linear Euler equations, in a conservative and perturbed form. The *sAbrinA* solver employs high-order finite difference operators, involving 6th-order spatial derivatives and 10th-order filters, as well as a 3rd-order compact Runge-Kutta explicit time-marching scheme. More detailed information about the *sAbrinA* solver and its underlying methodology can be found in [21, 22].

1. Acoustic mesh

As previously mentioned, in the CAA computations, the geometry of interest is taken into account with the IBM approach, which thus greatly simplifies the CAA mesh design process for such a geometry. The mesh consists in a single 3D Cartesian grid. A refined mesh zone was defined around the test bench up to the wind-tunnel walls and on the whole test section length by setting a maximum mesh size chosen to resolve the acoustic waves. Outside of the refined mesh zone, a grid stretching is applied with a geometrical ratio equal to $r = 1.05$ in the longitudinal direction to increase by a factor 20 the refined mesh size to the exit boundary conditions. No stretching was necessary for the two crosswise directions because no computation is performed outside of the wind-tunnel walls. The maximum cell size inside the refined mesh zone was calibrated from the target frequency associated to BPF2. 12 points per acoustic wavelength are considered for the latter frequency in the upstream and downstream directions, the rotor plane being the reference. The mesh size Δx, associated to the apparent wavelength due to the convection effects, is then $\Delta x = \lambda.(1 \pm \mathrm{M})/12$ with λ the wavelength at rest and M the Mach number. This gives a total number of points of 819×10^6.

As with the flow field, the same mesh is considered for both the confined and free-field configurations in order to remove the bias related to numerical precision linked with the mesh spacing. A sponge zone has nonetheless been added for the flow-field simulation in order to ensure that no spurious waves are reflected on the computational domain boundaries.

2. Numerical parameters

The time step Δt was chosen to get a maximum CFL number of about 0.76. Results and statistics are acquired over 5T once the convergence is reached (where T is the period associated to the frequency BPF1) after a numerical transient time of 100T for the confined simulation and 50T for the free-field one. The confined simulation required about 14×10^3 CPU hours (on 1530 parallel cores) whereas the free-field one required half this time. These computational times are rather inexpensive compared to computations with curvilinear and body-fitted meshes thanks to the IBM which enables to maximize the time step and thus to minimize the number of iterations for one period of the source, here: $\Delta t = T/60$. Furthermore, the IBM preprocessing was performed in less than 0.01% of the overall computational time.

C. Acoustic results

The acoustic field associated to each BPF can be easily obtained from a standard Fourier transform. The real part of the Fourier transform of the fluctuating pressure associated to BPF1 and BPF2 as well as the SPL amplitude are presented in figures 7 and 8 for both cases. Here, the left hand side of the figures represents the upstream direction and the right hand side the downstream direction. For rendering purposes, different colour scales have been considered for each group of figures. For figures 7 and 8, the pressure field has been restricted to the refined mesh zone as it has been checked that the pressure waves amplitudes are rapidly dissipated due to the grid stretching. Moreover, the white rectangle in the middle of the figures corresponds to the NRI surface inside of which acoustic levels should be nearly zero if the mean flow corresponded to the uniform flow prescribed in the source model.

A first observation of interest is the difference in the free-field radiation pattern between the two simulated frequencies, see figures 7(b,d) and 8(b,d). Indeed, the BPF2 pressure field contains more cut-on modes which produce more lobes in the directivity pattern (see the SPL amplitude levels): 3 main lobes and 3 secondary lobes compared to the 4 lobes of the BPF1 pressure field. Between the different lobes, strong interferences are visible. The different free-field radiation patterns suggest that the acoustic confinement effects will potentially not have the same impact on the two frequencies. Moreover, the pressure field amplitude may vary azimuthally*, with periodicity patterns $(2\pi/V)$ associated to the vane number (V) (e.g. see [10, 13, 17]) and attributed to interference effects between coherent interaction modes.

In figure 7(a,c), and similarly in figure 8(a,c), the confinement effect is clearly visible as the strong specular reflections on the wind-tunnel walls create complex acoustic interferences pattern which disturb the acoustic field especially close to the wind-tunnel wall. However, away from the wind-tunnel walls, the free-field acoustic field can still be distinguished, especially at BPF2, for the three main directions of radiation: upstream and downstream of the rotor plane, approximately at ±45°, and around the rotor plane.

Once the convergence is reached, Fourier transform of the pressure fluctuations at BPF1 and BPF2 are stored on acoustic antennae composed of a longitudinal line of microphones located at $2.5D_b$ of the rotor axis in the same

*the azimuthal angle corresponds to the angle of revolution around the rotor axis

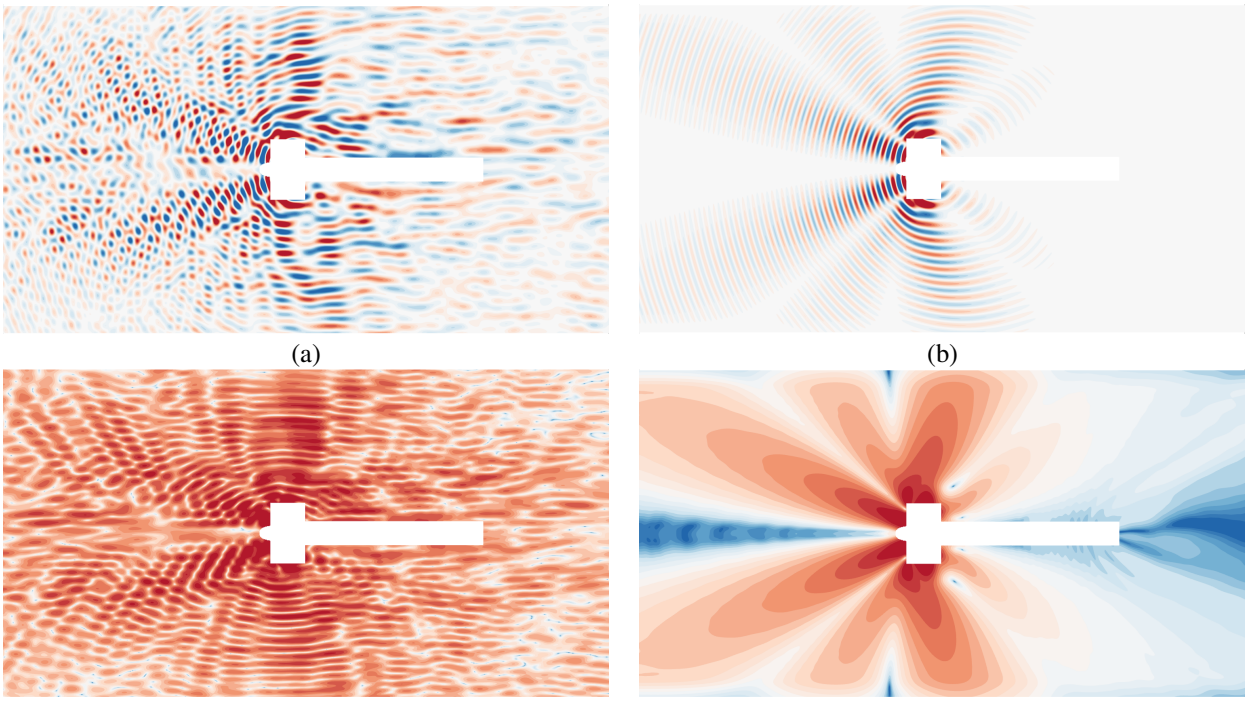

(a) (b)

(c) (d)

Fig. 7 Real part of the fluctuating pressure field associated to BPF1 (a,b) and SPL in dB (c,d) in a horizontal plane for the (a,c) confined configuration and (b,d) the free-field configuration.

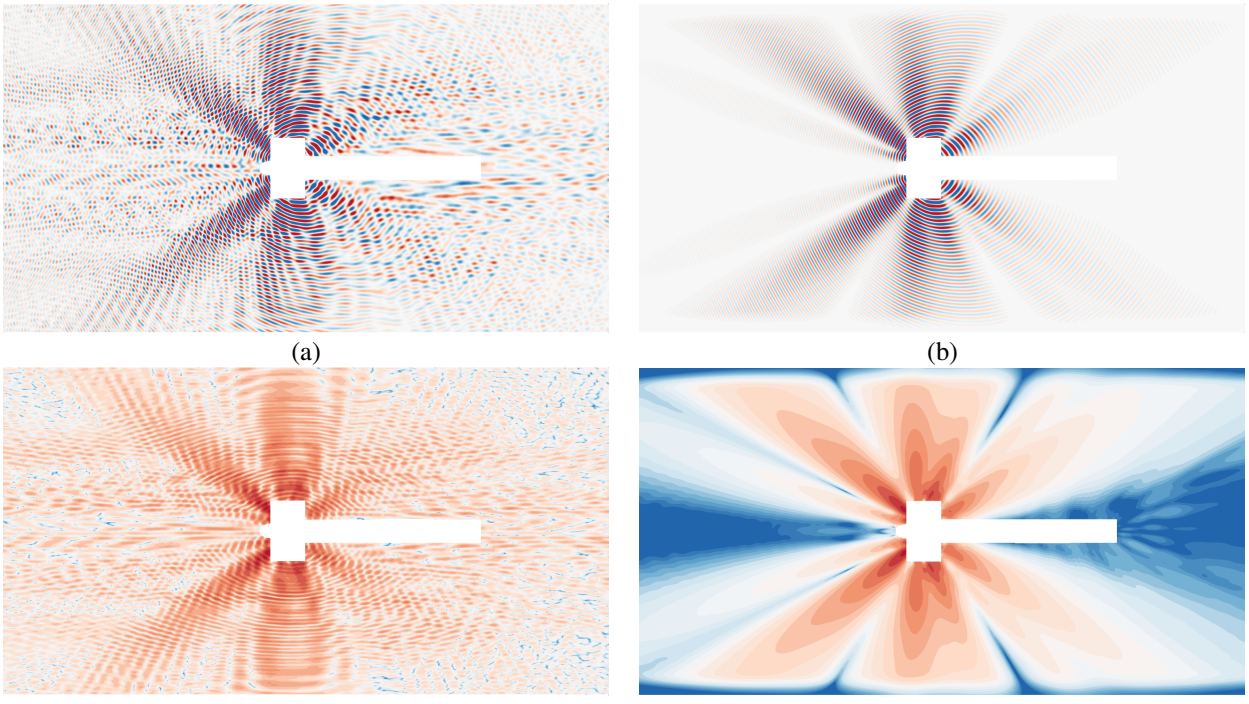

(a) (b)

(c) (d)

Fig. 8 Real part of the fluctuating pressure field associated to BPF2 (a,b) and SPL in dB (c,d) in a horizontal plane for the (a,c) confined configuration and (b,d) the free-field configuration.

horizontal plane. The evolution of the SPL along this antenna for the two simulated configurations is shown in figure 9

for both frequencies. In this figure, $\theta = 0°$ represents the rotor plane, $\theta \leq 0°$ represents the upstream direction and $\theta \geq 0°$ the downstream directions. As all the results are shown for only one frequency at a time, pronounced interference patterns with large variations of amplitude are visible in these figures, particularly for angles $|\theta| \geq 40°$.

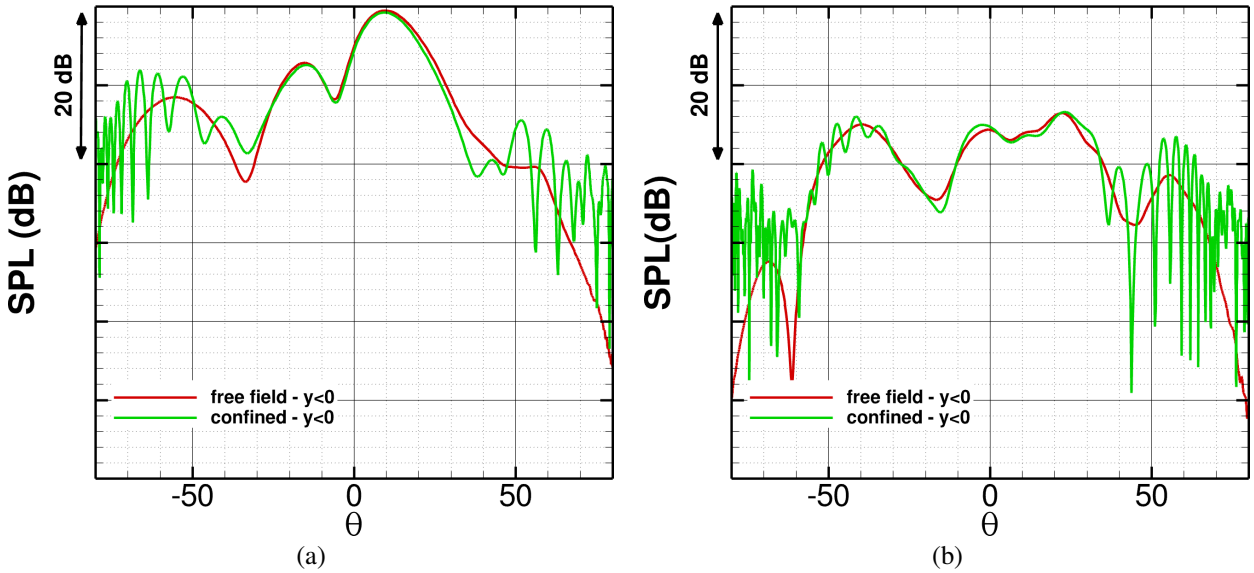

Fig. 9 Comparisons of the SPL (in dB) associated to BPF1 (a) BPF2 (b) on a longitudinal antenna located at $2.5D_b$ of the rotor axis in the same horizontal plane.

In these figures, it appears that, for both frequencies, the confined simulations give SPL levels close to the free-field ones in particular for angles $\theta \in [-30°; +30°]$, for the other angular positions, the large variations of amplitude related to the pronounced interference patterns lead to strong discrepancies between the two simulations. The angular positions for which there is a good agreement between the two simulations correspond to angular positions close to the rotor plane, i.e. where there are less reflected acoustic waves than for other positions. Furthermore, the longitudinal antenna is located approximately at $8D_b$ away from the wind-tunnel walls, i.e. more than three times the distance of the antenna from the rotor axis. Thus, for this antenna location and these angular positions, the reflected waves amplitude is sufficiently damped with respect to the direct source radiation to have only a small effect on the confined configuration measurements.

In summary, two acoustic simulations with realistic USF acoustic directivities at BPF1 and BPF2 as well as a generic test bench and wind-tunnel test section geometries and non uniform mean flow field have been performed. The simulations results show that despite the untreated wind-tunnel walls, it is possible to recover, at least for angular positions with dominant levels, the free-field configuration acoustic directivity. These findings are true for the studied configurations and the chosen antenna. This makes the numerical acoustic simulation a quite helpful tool for the acoustic qualification of prescribed test set-up and design of future experimental measurements.

V. Conclusions and perspectives

A numerical methodology has been developed to evaluate the confinement effects of USF noise in a closed wind-tunnel. This methodology is based on a USF source model which gives access to the tone noise radiation in the free field but limited to isolated open fan configurations in a uniform mean flow. To take into account for realistic flow convection and wind-tunnel walls, this model has been injected in ONERA's CAA solver *sAbrinA* which solves the Euler equations in 3D and can consider complex geometries via the Immersed Boundary Method (IBM) and non-uniform mean flows (e.g. issued from RANS simulations). The injection of the USF source model into *sAbrinA* requires the reconstruction of acoustic velocity from the acoustic pressure data. The reconstruction has been implemented and validated first on the academic monopolar source test case. Then the propagation of the reconstructed field by the CAA solver has been validated on inputs generated by the source model at BPF1 for an approach condition.

Two simulations have been performed to evaluate the acoustic confinement effects of a USF at BPF1 and BPF2 in a closed wind-tunnel for an operating point representative of a take-off condition: one in free-field and the other one in the wind-tunnel. Despite the strong specular reflections on the wind-tunnel walls leading to complex acoustic

interference patterns visible in the confined configuration, the free-field acoustic directivity can still be retrieved for particular angles, especially for microphones positions away from the wind-tunnel walls.

Given these first results at BPF1 and BPF2 at a relatively low Mach number, further work will consist in evaluating the methodology at higher frequencies and/or higher mean flow velocities. For cruise operating condition, shocks are present and require quadrupole terms which can be taken into account by a Ffowcs Williams and Hawkings porous surface formulation. The reconstruction method can also be applied to such data. Another aspect to look at in order to continue this study, would be to consider acoustically treated walls (at least partially) as was done in previous numerical study on fan noise confinement effects. Furthermore, it would be interesting to make use of phased microphone array processing techniques to widen the angular span on which the acoustic directivity is retrieved from the confined configuration pressure levels.

Acknowledgments

This work is supported by the project CLEOPATRA (CLEaner future through OPen fAn inTegRAtion) which has received funding from the French DGAC. The authors thank Jacky Mardjono from Safran Aircraft Engines for having provided the mean flow data.

References

[1] Mincu, D. C., Le Garrec, T., Péron, S., and Terracol, M., "Immersed boundary conditions for high order CAA solvers-Aeroacoustics installation effects assessment," *23rd AIAA/CEAS Aeroacoustics Conference*, 2017.

[2] Lorteau, M., Wiart, L., and Kopiev, V., "Numerical study, with experimental validation, of fan noise installation effects in Over-Wing Nacelle configuration using the Immersed Boundary Method," *25th AIAA/CEAS Aeroacoustics Conference*, 2019.

[3] Lorteau, M., and Le Garrec, T., "Numerical assessment of fan noise confinement effects in a closed wind-tunnel," *AIAA AVIATION 2021 FORUM*, Vol. (2302), 2021. doi:10.2514/6.2021-2302.

[4] Lorteau, M., Le Garrec, T., Daroukh, M., and Polacsek, C., "Acoustic assessment of BLI effects on Airbus Nautilius engine integration concept - part I: noise radiation," *28th AIAA/CEAS Aeroacoustics Conference*, Vol. (2992), 2022.

[5] Terracol, M., Manoha, E., Herrero, C., Labourasse, E., Redonnet, S., and Sagaut, P., "Hybrid method for airframe noise numerical prediction," *Theoretical and Computational Fluid Dynamics*, Vol. 19, 2005, pp. 197–227.

[6] Polacsek, C., Desquesnes, G., and Reboul, G., "An equivalent-source model for simulating noise generation in turbofan engines," *Journal of Sound and Vibration*, Vol. 323, 2009, pp. 697–717.

[7] Redonnet, S., Desquesnes, G., Manoha, E., and Parzini, C., "Numerical study of acoustic installation effects with computational aeroacoustics method," *AIAA Journal*, Vol. 48, No. 5, 2010, pp. 929–937.

[8] Reboul, G., and Polacsek, C., "Towards Numerical Simulation of Fan Broadband Noise Aft Radiation from Aero-engines," *AIAA Journal*, Vol. 48, No. 9, 2010, pp. 2038–2048.

[9] Redonnet, S., and Druon, Y., "Computational Aeroacoustics of Realistic Co-Axial Engines," *AIAA Journal*, Vol. 50, No. 5, 2012, pp. 1029–1046.

[10] Daydé-Thomas, V. and Polacsek, C. and Gloerfelt, X. and Sugiyama, M. and Mardjono, J., "Tone noise prediction of an open-fan engine using a source-mode integral formulation," *Forum Acusticum 2023*, 2023.

[11] Daydé-Thomas, V. and Polacsek, C. and Fauqueux, S. and Gloerfelt, X. and Mardjono, J., "Tone noise characterization of an open-fan engine using source-mode integral formulations," 30^{th} *AIAA/CEAS Aeroacoustics Conference*, Rome, Italy, 2024.

[12] Benoit, C., Péron, S., and Landier, S., "Cassiopee: A CFD pre- and post-processing tool," *Aerospace Science and Technology*, Vol. 45, 2015, pp. 272 – 283.

[13] Roger, M., and Kucukcoskun, K., "Near-and-far field modeling of advanced tail-rotor noise using source-mode expansions," *Journal of Sound and Vibration*, Vol. 453, 2019, pp. 328–354.

[14] Rahier, G., Prieur, J., Vuillot, F., Lupoglazoff, N., and Biancherin, A., "Investigation of integral surface formulations for acoustic post-processing of unsteady aerodynamic jet simulations," *Aerospace Science and Technology*, Vol. 8, 2004.

[15] Redonnet, S., Loackard, D., Khorrami, M., and Choudhari, M., "The non-reflective interface: an innovative forcing technique for computational acoustic hybrid methods," *International Journal of Numerical Methods in Fluids*, Vol. 81, 2016, pp. 22 – 24.

[16] Le Garrec, T., Polacsek, C., Chelius, A., Daroukh, M., and François, B., "Tone noise predictions of a full-scale UHBR engine at approach condition with inflow distortion effects," *25th AIAA/CEAS Aeroacoustics Conference*, Vol. (2606), 2019.

[17] Sugiyama, M., Falissard, F., Reboul, G., Jaouani, N., and Gloerfelt, X., "Noise prediction of an open fan using acoustic analogy approaches," *Inter Noise 2023*, 2023.

[18] Sugiyama, M., Jouani, N., Falissard, F., Reboul, G., and Gloerfelt, X., "Numerical investigation of Open Fan's tonal noise prediction in low and high speed condition," 30^{th} *AIAA/CEAS Aeroacoustics Conference*, 2024.

[19] Lewis, D., Falissard, F., and Perrin, C., "Tonal noise predictions of a generic Open-Fan based on a hybrid URANS approach," 30^{th} *AIAA/CEAS Aeroacoustics Conference*, 2024.

[20] Cambier, L., Heib, S., and Plot, S., "The Onera elsA CFD software: input from research and feedback from industry," *Mechanics & Industry*, Vol. 14, No. 3, 2013, pp. 159–174.

[21] Redonnet, S., Manoha, E., and Sagaut, P., "Numerical simulation of propagation of small perturbations interacting with flows and solid bodies," *AIAA paper*, Vol. (3493), 2001.

[22] Redonnet, S., "Simulation de la propagation acoustique en présence d'écoulements quelconques et de structures solides, par résolution numérique des équations d'Euler," Ph.D. thesis, Université Bordeaux 1, 2001.